

Local-Global Temporal Difference Learning for Satellite Video Super-Resolution

Yi Xiao, Qiangqiang Yuan , *Member, IEEE*, Kui Jiang, *Member, IEEE*, Xianyu Jin, Jiang He, Liangpei Zhang , *Fellow, IEEE*, and Chia-wen Lin , *Fellow, IEEE*.

Abstract—Optical-flow-based and kernel-based approaches have been widely explored for temporal compensation in satellite video super-resolution (VSR). However, these techniques involve high computational consumption and are prone to fail under complex motions. In this paper, we proposed to exploit the well-defined temporal difference for efficient and robust temporal compensation. To fully utilize the temporal information within frames, we separately modeled the short-term and long-term temporal discrepancy since they provide distinctive complementary properties. Specifically, a short-term temporal difference module is designed to extract local motion representations from residual maps between adjacent frames, which provides more clues for accurate textures representation. Meanwhile, the global dependency in the entire frame sequence is explored via the long-term difference learning. The differences between forward and backward segments are incorporated and activated to modulate the temporal feature, resulting in holistic global compensation. Besides, we further proposed a difference compensation unit to enrich the interaction between the spatial distribution of the target frame and compensated results, which helps maintain spatial consistency while refining the features to avoid misalignment. Extensive objective and subjective evaluation on five mainstream satellite videos demonstrate that the proposed method performs favorably for satellite VSR. Code will be available at <https://github.com/XY-boy/TDMVSR>.

Index Terms—Satellite video, super-resolution, temporal difference, global-local compensation, remote sensing.

I. INTRODUCTION

SATELLITE video, an emerging datasource captured by aerial video sensors, allows for continuous remote sensing observation of a specific area. Compared to static remote sensing images, satellite video increases the temporal resolution by a large margin from 'days' to 'seconds'. Therefore, it has

This work was supported in part by the National Natural Science Foundation of China under Grant 41922008 and 61971319. (Corresponding author: Qiangqiang Yuan.)

Yi Xiao is with the School of Geodesy and Geomatics, Wuhan University, Wuhan 430079, China (e-mail: xiao_yi@whu.edu.cn).

Qiangqiang Yuan is with the School of Geodesy and Geomatics, Wuhan University, Wuhan 430079, China (e-mail: yqiang86@gmail.com).

Kui Jiang is with the Cloud BU, Huawei Technologies, Hangzhou 310000, China (e-mail: kuijiang_1994@163.com).

Xianyu Jin is with the School of Geodesy and Geomatics, Wuhan University, Wuhan 430079, China (e-mail: jin_xy@whu.edu.cn).

Jiang He is with the School of Geodesy and Geomatics, Wuhan University, Wuhan 430079, China (e-mail: jiang_he@whu.edu.cn).

Liangpei Zhang is with the State Key Laboratory of Information Engineering in Surveying, Mapping, and Remote Sensing, Wuhan University, Wuhan 430079, China (e-mail: zlp62@whu.edu.cn).

Chia-Wen Lin is with the Department of Electrical Engineering and the Institute of Communications Engineering, National Tsing Hua University, Hsinchu 30013, Taiwan (e-mail: cwlin@ee.nthu.edu.tw).

been widely applied to dynamic applications such as change detection [1], object tracking [2], and traffic monitoring [3].

However, limited by ultra-remote imaging and transmission bandwidth, the acquired satellite video commonly are far from meeting the application requirements due to the inevitable degradation. Rather than improving hardware, super-resolution (SR) technologies provide a more optimal scheme. Prior to deep neural networks, the early model-based SR methods rely more on statistical analyses of image contents, and enforce handcrafted priors to reconstruct more plausible details. However, they are not robust to large-scale or complex imaging scenarios, satellite image in particular. By contrast, convolution neural networks (CNNs) [4], [5] have emerged as a preferable choice due to the powerful non-linear representation ability. Both image or video SR, there is increasing attention developed to promoting the SR performance [6]–[11].

Different from single-image super-resolution, VSR can explore more complementary temporal information within video frames to ease the ill-posed problem. Therefore, compensating the temporal information of misaligned inter-frames is vital for VSR. Most previous works are mainly engaged in optical flow [12]–[14] and kernel estimation [15], [16] for motion compensation. The optical-flow-based methods often employ an extra component to get the flow maps between frames or jointly optimize the flow estimation sub-network with the whole network. However, flow estimation is a laborious task and would introduce high complexity. The kernel-based methods, *e.g.*, 3D convolution [17], [18] and deformable convolution (DConv) [19], either ignore the valuable temporal priors or have limited spatial-temporal receptive field. Moreover, these approaches are easily collapsed in complex motion. Recently, several works [20]–[22] proposed to propagate rich historical information recurrently. Nevertheless, they acquire a considerable memory cost to cache future and past frames.

In contrast to natural video, satellite video has some characteristics that make temporal compensation more complicated. For instance, the background of a remote-sensing image usually covers most of the area, while the moving foreground only occupies a few pixels. Therefore, optical flow estimation and DConv inevitably involve redundant calculations. Furthermore, due to the complex landcover type in a wide-range remote sensing image, the object scale varies from different patches, especially the multi-scale moving objects. In this case, establishing an efficient and straightforward solution to model the motion information in satellite videos remains a challenging problem.

Although remarkable progress has been made in temporal

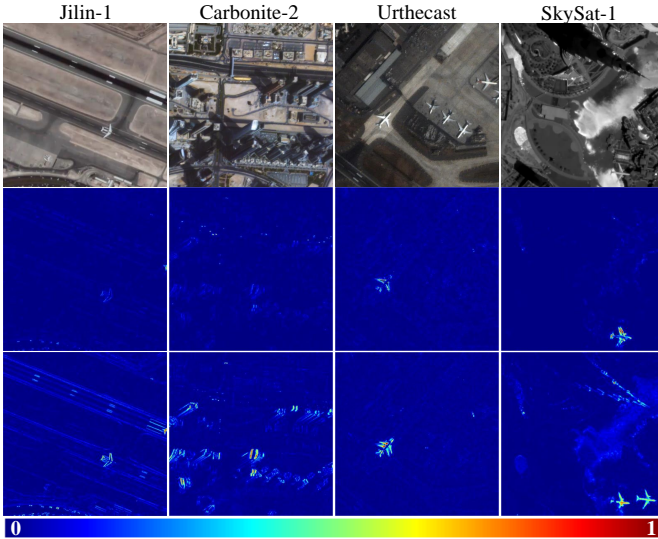


Fig. 1. The RGB temporal difference maps between the target frames (the first row) and neighboring frames. These sparse signals exhibit low values for major areas. Besides, the short-term temporal difference (the second row) and Long-term temporal difference (the third row) reflect a different level of difference.

information compensation, few studies have examined the temporal difference among inter-frames in satellite VSR. Recently, the explicit temporal difference was explored in high-level video tasks [23], [24]. These studies have argued that the RGB difference is informative to model motion information and can be an alternative to optical flow. This motivates us to exploit temporal differences among frames to realize temporal compensation because generating temporal differences is naturally well-defined and effortless. What's more, temporal difference maps of remote sensing images are sparse because the massive redundancy (highly similar background across frames) will be reduced to low values after subtraction. The high response of difference map focuses on the changed part between frames, where these parts are usually corresponding to object motion and boundary tremor. Fig. 1 shows some temporal difference maps where the motion information is well-activated. Besides, we found the short-term temporal difference is prominent on the boundary of moving objects, and the long-term temporal difference contains more edge and shape information. Thus, they can not be treated equally because of the distinctive levels of difference.

To investigate the potential of explicit temporal difference in satellite VSR, this paper proposed a global-local temporal difference learning network (TDMVSR) to systematically exploit the global-local complementary information. Instead of directly computing the difference maps between the target and neighboring frames, we proposed fully utilizing the temporal difference at local and global distributions. In particular, our Short-term Temporal Difference Modeling branch (S-TDM) derives the local information from adjacent frames with low variance, while the global information with large variance is inferred by a Long-term Temporal Difference Modeling branch (L-TDM). In S-TDM, the RGB difference maps will be converted to local motion representations and supplied to target feature with lateral connections. Besides, L-TDM is responsible for activating the motion variations from future

and past frames through forward and backward propagation. To alleviate the misalignment caused by temporal modeling, we increase the interaction between the target frame and temporal information yielded from TDMs. The outputs of S-TDM and L-TDM will successively be fed into a Difference Compensation Unit (DCU) to enrich and refine the spatial feature. In this manner, our S-TDM and L-TDM will focus on valuable information to reconstruct the target frame and maintain spatial consistency. In short, our contributions are as follows:

- 1) We proposed to exploit the long-short term inter-frames temporal difference to realize information compensation for satellite VSR.
- 2) Our S-TDM and L-TDM could systematically utilize local and global complementary information from distinctive motion patterns.
- 3) The proposed DCU could excavate valuable information and maintain spatial consistency.
- 4) Compared with optical-flow-based and kernel-based approaches, our TDMVSR achieves favorable quantitative and qualitative results on five mainstream satellite video data sources.

The remainder of this paper is organized as follows: Section II reviews video super-resolution, Section III involves details of the proposed method, Section IV contains experiments and analysis, and Section V is conclusion.

II. RELATED WORK

A. Video Super-Resolution

Here, we first review optical flow-based VSR methods that employ optical flow to describe motion information followed by explicit motion compensation. Then, we present kernel-based implicit alignment methods. Finally, we introduce the recurrent propagation VSR framework.

1) *Optical-flow-based VSR methods*: Generally, the flow estimation algorithms can be divided into traditional and deep-learning. In the traditional approach, Deep-DE [25] used ℓ_1 flow [26] to generate a series SR drafts, then the bilinear upsampled LR target frame is concatenated with these drafts and sent to CNN and deconvolution layer for reconstruction. VSRNet [27] adopted Drudeas algorithm [28] to compute the flow maps and proposed a filter symmetry mechanism to compensate neighboring frames. Recently, Haris *et al.* [12] put forward a recurrent back-projection network (RBPN), where the flow estimation is employed by an external package named Pyflow [29]. The deep-learning-based flow estimation often relies on CNN to predict flows. For instance, Caballero *et al.* [30] developed a motion compensation transformer (MCT) to learn the motion information and perform motion compensation simultaneously. After that, they passed the compensated features to spatial-temporal ESPCN. To mitigate the resolution gap between low-resolution flow maps and latent high-resolution features, Wang *et al.* [13] designed a unified framework to jointly super-resolve optical flow maps and target frame. In addition to this, some elaborate networks such as FlowNet [31] and SpyNet [32] are widely used CNN architecture for optical flow estimation.

However, neither traditional nor deep-learning estimation can not guarantee the accuracy of flows, especially under the challenge of complex and large motion. The model will suffer from severl performance drop due to the inaccuracy flow estimation. Besides, the use of external alogrithm and specific sub-network will inevitably increase the computation consumption.

2) *Kernel-based VSR methods*: This kind of approach usually implicitly parameterizes the temporal compensation into convolution kernels, with typical efforts on 3D convolution [33], non-local module [34], and deformable convolution (DConv). Jo *et al.* [18] learned a 3D dynamic upsampling filter (DUF) for each pixel to avoid explicit motion estimation and compensation. Kim *et al.* [33] employed 3D convolution (3DSRNet) for spatial-temporal modeling. However, 3D convolution is not sophisticated enough to model the temporal priors and would increase the complexity as well. Non-local-based approaches hire the non-local attention mechanism to capture long-range dependencies, which increase the receptive field of temporal information. Yi *et al.* [34] proposed a progressive fusion strategy to aggregate the non-local spatial-temporal information. Yu *et al.* [15] established a novel cross-frame non-local attention and memory-augment attention (MANA) to memory details cross-frames. Nevertheless, non-local learning introduces a significant inference complexity and gains limited improvement. The DConv is first proposed in [35] and carried forward by many works like TDAN [36], EDVR [16], and D3DNet [37]. The key to DConv is attaining the offset parameters and aplling them on the convolution grid to yield a deformable sampling position. Hence, the convolution can involve motion information inside the receptive field. TDAN [36] used shallow convolution layers to predict the offsets. EDVR [16] enlarged the receptive field with the help of a pyramid structure and coarse-to-fine alignment. D3DNet introduced DConv to 3D dimension for a larger temporal receptive field.

Although kernel-based methods bring promising improvements, they still face harsh convergence conditions and inefficient computation.

3) *Recurrent propogation VSR methods*: Such methods aim to fully utilize the long-range dependencies by propagating rich future or past information in a recurrent manner. For example, Huang *et al.* [38] proposed a recurrent bidirectional network with forward and backward subnetworks. The two similar subnetworks are responsible for learning the previous and past frames. In [39]–[41], the authors employ LSTM to leverage the long-distance temporal properties. While the RNN-based network is suitable for spatial-temporal modeling, the errors caused by misalignment may accumulate with the input length increase. Toward this end, Chan *et al.* [20] come up with an information-refill and propagation strategy to ease the misalignment accumulation. In addition, they enhance the interaction of bi-directional temporal information by forward and backward propagation. Recently, Yi [21] exploited all of the neighboring frames as auxiliary information to further enhance the recurrent propagation. More recently, BasicVSR++ [42] is proposed to strengthen the alignment and propagation process.

To sum up, recurrent propagation VSR methods can benefit from RNNs or LSTMs to capture the long-range dependency with a lightweight design. However, it is hard to train an RNN due to the gradient vanishing. Furthermore, they still lack of using short-term information between adjancent frames, since recurrent structures naturally focus on long-term information.

B. Satellite Video Super-resolution

In satellite VSR, early efforts [43] often transfer the single-image super-resolution (SISR) frameworks on satellite video without specific consideration of the characteristics of remote sensing imagery. Later, more methods applicable to remote sensing images were explored. Jiang *et al.* [44] proposed a GAN-based framework to enhance the high-frequency edge information. Zhang *et al.* [45] take account for scene variation in remote sensing images and put forward a scene-adaptive strategy to alleviate the performance drop across scenes. He *et al.* [46] proposed a hybrid-scale network to fully extracted the multi-scale information. However, these methods are SISR, thus failing to model the temporal information and having a bottleneck. Recently, Liu *et al.* [47] designed a traditional method, which adaptively examined the non-local similarity in wide-range remote sensing imagery. He *et al.* [48] proposed to employ 3D convolution to implicitly achieve motion compensation. But it increases computational consumption and has gained limited performance without sophisticated design. More recently, Xiao *et al.* [19] proposed a multi-scale DConv model for precise alignment and designed a temporal grouping projection to realize effective spatial-temporal fusion.

Years of effort have witnessed remarkable progress in satellite VSR, but we still need an efficient and straightforward solution to excavate the high-redundant temporal information in satellite video.

III. METHODOLOGY

A. Overview

The overall flowchart of our proposed framework is shown in Fig. 2. Given $2N + 1$ LR inputs $I = \{I_{t-N}, \dots, I_t, \dots, I_{t+N}\}$, I_t is the target frame required to be super-resolved, and the remaining frames are neighboring frames. We designed two branches to explore global-local complementary information separately by L-TDM and S-TDM. The difference compensation unit is intended to realize the interaction between temporal information yield from TDMs and the spatial feature. The compensated feature will be sent to the reconstruction module to generate the final super-resolved target frame I_t^{SR} .

S-TDM, termed $TDM_s(\cdot)$, receives frame-wise inputs I and output the short-term compensated results g_s , that is:

$$g_s = TDM_s(I), \quad (1)$$

The spatial feature F_t is extracted from I_t by a 3×3 convolution layer. F_t and g_s will be sent to difference compensation unit $DUC(\cdot)$ to refine the compensated g_s with the guide of F_t , thus we can maintain the spatial consistency and alleviate

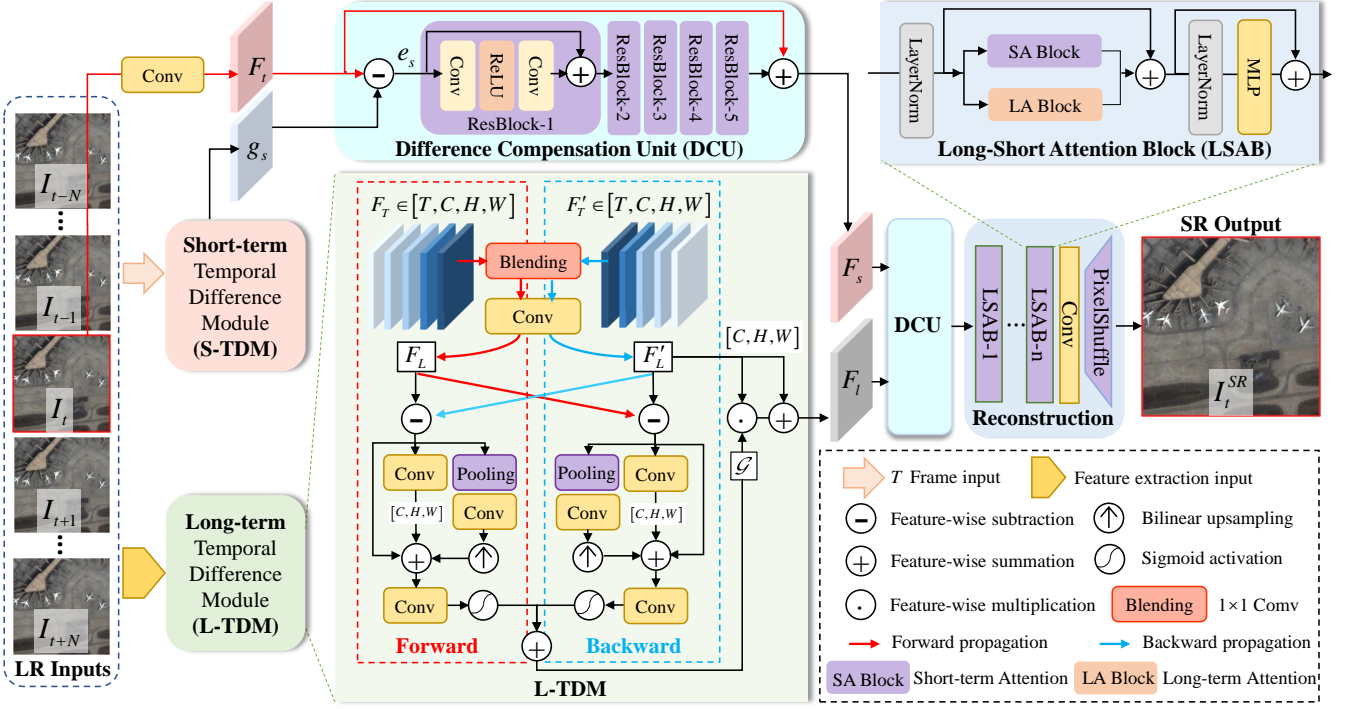


Fig. 2. The overall structure of our proposed global-local temporal difference learning network (TDMVSR). It consists of four modules: (1) Short-term Temporal Difference Module (S-TDM), which is used for local temporal compensation; (2) Long-term Temporal Difference Module, which is proposed to realize global temporal compensation; (3) Difference Compensation Unit (DCU), which is adopted for integrating the spatial and temporal information to maintain the spatial consistency; (4) Reconstruction module, which is employed to generate the final HR target frame.

the misalignment in S-TDM. The refinement process can be written as:

$$F_s = \text{DUC}(F_t, g_s), \quad (2)$$

where F_s is the short-term temporal compensated feature. L-TDM received $T = 2N + 1$ features to explore the global temporal difference. Here, we use five residual blocks to extract T features from I . Take the forward branch in L-TDM as an example, T features will be blended by a 1×1 convolution layer and another 3×3 convolution. In this manner, we can smooth the long-range features to get a holistic representation F_L of the forward features. Similarly, we obtain the backward global feature F'_L from F'_T , where F'_T is the temporal reverse version of F_T . Thanks to L-TDM, we implicitly produce a temporal activation \mathcal{G} for temporal compensation. The global temporal compensation result F_l is determined by:

$$F_l = F'_T \odot \mathcal{G} + F'_T, \quad (3)$$

where \odot is the channel-wise multiplication. After that, the F_l will also be refined by DUC with the guide of F_s . The final global-local temporal compensated feature \hat{F}_t can be generated by the following:

$$\hat{F}_t = \text{DUC}(F_s, F_l). \quad (4)$$

Finally, \hat{F}_t will be reconstructed to I_t^{SR} by the reconstruction module Reconstruction (·):

$$I_t^{SR} = \text{Reconstruction}(\hat{F}_t). \quad (5)$$

B. Short-term Temporal Difference Module

Generally, adjacent frames have high redundancy, and directly concatenating the local frames for compensation is inefficient. Therefore, we choose to supply the target frame with several short-term temporal differences to yield an efficient local temporal information compensation.

Specifically, S-TDM operates feature extraction from short-term RGB difference maps between adjacent frames and propagates local motions into the target feature with lateral connections. As shown in Fig. 3., for simplicity, we set $N = 2$. Firstly, we compute four temporal differences by subtracting adjacent frames. Then we extract features from these RGB differences and reduce them to low-resolution space. In this manner, we could obtain four representations $\{d^{-2}, d^{-1}, d^{+1}, d^{+2}\}$ of local motions.

As mentioned before, short-term RGB temporal differences have overwhelmingly low response regions and are prominent in motion pixels. Therefore, we argue that RGB differences are sparse signals and it is sufficient to process them in low-resolution space. In addition, we can reduce the computational cost of further temporal difference fusion by the pooling operation. To make the target feature f_t aware of short-term motion, we use a two-stage compensation strategy and supply f_t with lateral connections. In the early stage, the fused temporal representation D_s will be upsampled to the original size and added to the target features, which can be expressed as:

$$f_1 = f_t + \text{Up}^\uparrow(\text{Fusion}([d^{-2}, d^{-1}, d^{+1}, d^{+2}])), \quad (6)$$

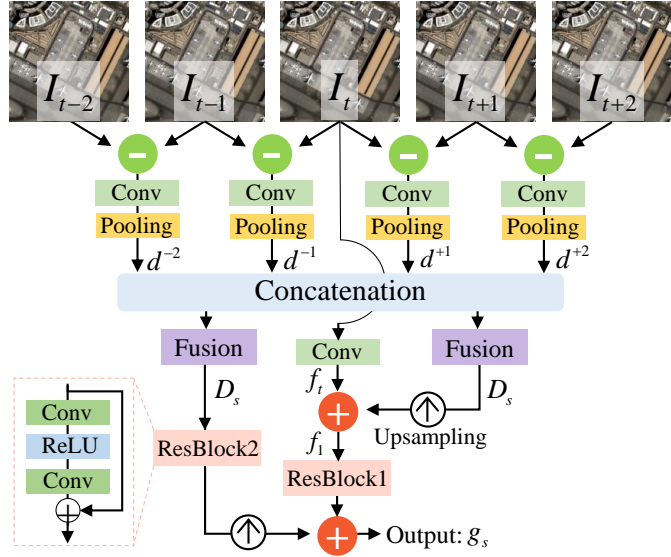


Fig. 3. The diagram of our proposed Short-term Temporal Difference Module (S-TDM). Here, we take $N = 2$ as an example. S-TDM operates feature extraction on the stacked RGB difference maps and supplies the local motions into the target feature for local compensation.

where Up^\uparrow denotes $\times 2$ bilinear upsampling, $\text{Fusion}(\cdot)$ represents a 3×3 convolution layer, and $[\cdot]$ is channel concatenation. In the second stage, the fused representation D_s and f_1 will be further extracted for deep aggregation. Finally, the short-term compensated feature g_s can be written as:

$$g_s = \text{Res}_1(f_1) + \text{Up}^\uparrow(\text{Res}_2(D_s)), \quad (7)$$

where $\text{Res}_1(\cdot)$ and $\text{Res}_2(\cdot)$ are two residual blocks.

C. Long-term Temporal Difference Module

Although S-TMD is capable of modeling local motion information from inter-frame RGB difference, it can not leverage the long-range dependency limited by the local receptive field. Therefore, our L-TMD is responsible for capturing the temporal information in the entire sequences by bidirectional temporal difference learning.

To handle the large motion while mitigating the misalignment within long-distance frames, we employ a shadow alignment operation through our previous Multi-Scale DConv alignment module [19]. Thus, the coarsely aligned feature F_T and F'_T could be compressed to smooth the large variance. Furthermore, the temporal difference is calculated between F_T and F'_T , *i.e.*, $D_f = F_L - F'_L$ and $D_b = F'_L - F_L$. This cross-difference operation encourages forward and backward branches to utilize complementary information in different segments.

During the succeeding propagation, a multi-scale design is employed to better preserve the multi-scale information in satellite video. In particular, three operations at different scales will be applied to the global temporal differences D_f and D_b : (1) Identification connection to stabilize the gradient; (2) Deep feature extraction on the original scale by a 3×3 convolution; (3) Feature propagation in a small-to-large scale, achieved by a pooling layer, a 3×3 convolution and a bilinear upsampling.

Algorithm 1: Global-local Temporal Difference Learning Algorithm.

Input: LR frames $I = \{I_{t-N}, \dots, I_t, \dots, I_{t+N}\}$.
Output: The super-resolved target frame I_t^{SR}

1 **Initialization:** $N = 5$, $S = 3$, $\sigma(\cdot)$ is 1×1 convolution, $\alpha = \beta = 0.5$.
// Short-term Temporal Difference
2 $f_t = \text{Conv}(I_t)$;
3 **for** $i = -N : +N$ and $i \neq 0$ **do**
4 **if** $i < 0$ **then**
5 $d^i = \text{Pooling}(\text{Conv}(I_{t+i} - I_{t+i+1}))$;
6 **else**
7 $d^i = \text{Pooling}(\text{Conv}(I_{t+i} - I_{t+i-1}))$;
8 **end**
9 **end**
10 $D_s = \text{Conv}([d^{-N} : d^{-N}])$; // Local motion
11 $f_1 = f_t + \text{Up}^\uparrow(D_s)$; // One stage
12 $g_s = \text{Res}_1(f_1) + \text{Up}^\uparrow(\text{Res}_2(D_s))$; // Two stage
// Coarse Alignment
13 $F_T = \text{MSD}(\text{Conv}(I))$, $F'_T = \text{reverse}(F_T)$; // Long-term Temporal Difference
14 $F_L = \text{Conv}(\sigma(F_T))$, $F'_L = \text{Conv}(\sigma(F'_T))$;
15 $D_f = F_L - F'_L$, $D_b = F'_L - F_L$;
16 $att_f = \text{Sigmoid} \left(\text{Conv} \left(\sum_{i=1}^S H_i(D_f) \right) \right)$,
17 $att_b = \text{Sigmoid} \left(\text{Conv} \left(\sum_{i=1}^S H_i(D_b) \right) \right)$;
18 $\mathcal{G} = \alpha * att_f + \beta * att_b$; // Global motion
19 $F_l = F'_L \odot \mathcal{G} + F'_L$;
// Refinement
20 $F_t = \text{Conv}(I_t)$;
21 $F_s = F_t + \text{ResNet}(F_t - g_s)$;
22 $\hat{F}_t = F_s + \text{ResNet}(F_s - F_l)$;
// Reconstruction
23 $I_t^{SR} = \text{Upsample} \left(\text{Conv} \left(\text{LSAB}^N \left(\hat{F}_t \right) \right) \right)$.

The outputs of three operations will be aggregated and sent to a convolution layer and sigmoid function for activation:

$$att_f = \text{Sigmoid} \left(\text{Conv} \left(\sum_{i=1}^3 H_i(D_f) \right) \right), \quad (8)$$

$$att_b = \text{Sigmoid} \left(\text{Conv} \left(\sum_{i=1}^3 H_i(D_b) \right) \right), \quad (9)$$

where H_i represents the i -th operations mentioned above. att_f and att_b are the activated maps in forward and backward branches. We composed att_f and att_b to obtain a final activation \mathcal{G} , that is:

$$\mathcal{G} = \alpha * att_f + \beta * att_b, \quad (10)$$

where α and β are two balance coefficient. Here we set $\alpha = \beta = 0.5$. In the end, the long-term temporal compensated feature F_l is generated by feature modulation:

$$F_l = F'_L \odot \mathcal{G} + F'_L, \quad (11)$$

where \odot is channel-wise multiplication.

D. Difference Compensation Unit

Benefit from our S-TDM and L-TDM, we can systematically explore global and local temporal information. However, there are still misalignments due to our temporal difference learning. Towards this end, the compensated feature F_s and F_l need further refinement to compensated valuable information to spatial feature F_t of target frame and maintain the spatial consistency. Here, we design a difference compensation unit to iterat the spatial-temporal information. As shown in Fig. 2, by predicting the difference feature between spatial feature F_t and short-term temporal compensated feature g_s , the residual feature e_s will be further enhanced and supplied to F_t . In this manner, the S-TDM will forced to focus on the valubale compensation information of F_t . The difference compensation between F_t and g_s can be summarized as:

$$F_s = F_t + \text{ResNet}(F_t - g_s), \quad (12)$$

Similarly, F_s will be compensated by F_l for the final refinement:

$$\hat{F}_t = F_t + \text{ResNet}(F_t - F_l), \quad (13)$$

Here $N = 5$ denotes the number of residual blocks.

E. Reconstruction

After short-term and long-term temporal information compensation, the spatial-temporal information is entangled. Therefore, we can not reconstruct the compensated feature with a naive design, such as using residual blocks. Nowadays, the attention mechanism has been widely used in super-resolution reconstruction, with the success of channel attention (CA) in RCAN [49] and multi-head self-attention (MSA) in SwinIR [50]. Previous work [51] has demonstrated that CA and MSA are experts in learning short-term and long-term dependencies, respectively. Here, we comfortably adopt the widely used CA and MSA to reconstruct the entangled global-local information in a hybrid design. In Fig. 2, the short-term attention block (SA Block) is employed by the CA module in RCAN, and the long-term attention block (LA Block) is equipped with MSA in SwinIR. Finally, five Long-Short Attention Blocks (LSAB) and a pixelshuffle layer are stacked to restore the super-resolved target frame:

$$I_t^{SR} = \text{Upsample} \left(\text{Conv} \left(\text{LSAB}^N \left(\hat{F}_t \right) \right) \right). \quad (14)$$

IV. EXPERIMENT AND DISCUSSION

A. Satellite Video Datasource

To comprehensively evaluate our TDMVSR, we collected extensive satellite video clips from five mainstream satellites, including Jilin-1, Carbonite-2, Urthecast, SkySat-1, and Zhuhai-1. Following our previous work [19], we cropped 189 clips of 640×640 from Jilin-1 to build the training set. Five scenes are randomly cropped from two Jilin-1 videos to build the test set Jilin-T. Besides, we additionally crop four scenes from Carbonite-2 and Urthecast, respectively. In

SkySat-1 and Zhuhai-1, two and one scenes are selected for further testing. Eventually, we have 189 video clips used for model training and 16 scenes from five satellites to evaluate model performance. The training and test sets can be found at <https://github.com/XY-boy/MSDTGP>

B. Implementation Details

Denoting the size of I_t^{SR} is $Hr \times Wr \times c$, where $c = 3$ means the RGB channels, H and W represent the height and width of LR input, and r is the scale factor. In this paper, we only focus on $r = 4$. The number of input LR frames is set to 5. During model training, we sample 4 LR video patches with size 64×64 of the bicubic downsampled HR counterparts in each minibatch. Data augmentation is realized on LR inputs by random flip and rotation. The initial learning rate is set to 1×10^{-4} and decays to half the previous one when it reaches every ten epochs. To minmize the $\mathcal{L}_1 = \|I_t^{SR} - I_t^{GT}\|_1$ distance between I_t^{SR} and ground-truth frame I_t^{GT} , the Adam optimazation with $\beta_1 = 0.9$ and $\beta_2 = 0.999$ was used. We trained our model on a single NVIDIA RTX 3090 for 50 epochs, and it took us nearly 40 hours on model training.

C. Comparison With State-of-the-Arts

We compared the proposed TDMVSR with state-of-the-art approaches, including TDAN [36], DUF-52L [18], RBPN [12], EDVR-L [16], SOF-VSR [13], MSDTGP [19], MANA [15], and BasicVSR [20]. For a fair comparison, we retrained these methods on the Jilin-1 training set following their official implementation. The PSNR and SSIM are used as objective metrics to evaluate the fidelity of the restored results. Note that the PSNR is calculated on the luminance (Y) channel, and we crop 8 pixels on the boundary as [18].

1) *Quantitative Evaluation*: As summarized in Table. I, II, III, the proposed TDMVSR achieved the best performance in five mainstream satellite videos. This demonstrates the effectiveness of global-local temporal difference learning for satellite VSR. Besides, it illustrates the good generalization of our TDMVSR on various satellites. In particular, our TDMVSR outperforms the flow-based method SOF-VSR 0.3dB and the kernel-based method EDVR-L 0.17dB on the Jilin-T in Table.I. Compared with the recurrent-based approach BasicVSR, we can still perform favorably with fewer input frames (5 frames v.s. 15 frames). These results prove that our S-TDM and L-TDM can explore sufficient temporal information even in a local window.

In Table. II, we found that EDVR-L and BasicVSR yield approaching performance. Although the recurrent propagation-based method enlarges the temporal receptive field compared with the window-slide approach, it still can not significantly improve while consuming more frames as input. Our TD-MVSR can lead BasicVSR to 0.18dB in Carbonite-2 and 0.1dB in Urthecast, demonstrating that the proposed L-TDM can explore long-range dependency effectively compared with recurrent structure. What's more, EDVR-L achieves the second performance on SkySat-1 and Zhuhai-1 in Table. III. This indicates the DConv-based alignment method could generalize better than recurrent propagation in some scenes. We speculate

TABLE I. Quantitative comparisons on Jilin-T. The PSNR/SSIMs are calculated on the luminance channel (Y). The FLOPs are computed on LR inputs with the size of 160×160 . Note that BasicVSR is a recurrent propagation method. Here the propagate length is set to 15. The best and second performances are highlighted in red and blue, respectively.

Method	Frames	#Param. (M)	FLOPs (G)	Scene-1	Scene-2	Scene-3	Scene-4	Scene-5	Average
Bicubic	-	-	-	31.05/0.9097	28.57/0.8630	30.62/0.9009	33.72/0.9391	32.47/0.9246	31.29/0.9075
TDAN [36]	5	1.97	-	35.32/0.9577	31.72/0.9255	34.08/0.9477	38.43/0.9727	36.37/0.9626	35.18/0.9532
DUF-52L [18]	7	6.8	736.6	35.83/0.9604	32.29/0.9326	34.57/0.9525	39.15/0.9761	36.88/0.9659	35.74/0.9575
RBPN [12]	7	12.8	3785.3	35.73/0.9595	32.10/0.9307	34.65/0.9534	39.26/0.9767	36.90/0.9660	35.73/0.9573
EDVR-L [16]	5	20.7	897.8	36.05/0.9620	32.45/0.9353	34.87/0.9554	39.37/0.9769	36.82/0.9660	35.91/0.9591
SOF-VSR [13]	3	1.06	127.3	35.89/0.9610	32.26/0.9328	34.70/0.9537	39.15/0.9760	36.88/0.9660	35.78/0.9579
MSDTGP [19]	5	14.1	1579.8	36.13/0.9631	32.42/0.9350	34.81/0.9551	39.46/0.9773	37.10/0.9675	35.98/0.9600
MANA [15]	7	22.2	633.5	35.94/0.9616	32.43/0.9347	34.78/0.9544	39.34/0.9768	37.03/0.9670	35.90/0.9589
BasicVSR [20]	15	6.3	163.7	36.14/0.9631	32.60/0.9372	34.87/0.9551	39.40/0.9770	37.19/0.9677	36.04/0.9601
TDMVSR (Ours)	5	20.1	647.8	36.21/0.9636	32.58/0.9369	34.93/0.9559	39.47/0.9773	37.22/0.9682	36.08/0.9604

TABLE II. Quantitative comparisons on Carbonite-2 and Urthecast. The best and second performances are highlighted in red and blue, respectively.

Data Source	Method	Scene-6	Scene-7	Scene-8	Scene-9	Average
Carbonite-2	Bicubic	39.23/0.9443	36.68/0.9201	32.25/0.8754	35.59/0.9271	35.94/0.9167
	DUF-52L [18]	41.47/0.9623	39.14/0.9471	34.74/0.9208	38.43/0.9528	38.45/0.9458
	SOF-VSR [13]	41.32/0.9611	38.96/0.9456	34.55/0.9178	38.20/0.9514	38.26/0.9440
	RBPN [12]	41.44/0.9624	39.04/0.9465	34.92/0.9237	38.58/0.9537	38.50/0.9466
	EDVR-L [16]	41.59/0.9632	39.21/0.9477	35.09/0.9251	38.66/0.9545	38.64/0.9476
	MSDTGP [19]	41.56/0.9630	39.00/0.9461	34.85/0.9225	38.48/0.9532	38.47/0.9462
	MANA [15]	41.66/0.9634	39.12/0.9470	34.89/0.9224	38.66/0.9541	38.58/0.9468
	BasicVSR [20]	41.64/0.9634	39.21/0.9478	35.10/0.9266	38.83/0.9550	38.70/0.9482
	TDMVSR (Ours)	41.73/0.9643	39.52/0.9516	35.27/0.9302	38.90/0.9557	38.86/0.9504
Data Source	Method	Scene-10	Scene-11	Scene-12	Scene-13	Average
UrtheCast	Bicubic	43.86/0.9917	25.32/0.7242	33.43/0.9130	45.20/0.9939	36.95/0.9057
	DUF-52L [18]	46.12/0.9939	26.66/0.7964	35.51/0.9407	47.57/0.9958	38.97/0.9317
	SOF-VSR [13]	45.68/0.9934	26.67/0.7934	35.46/0.9397	46.70/0.9952	38.63/0.9304
	RBPN [12]	45.84/0.9936	26.66/0.7965	35.43/0.9404	47.14/0.9954	38.77/0.9315
	EDVR-L [16]	46.10/0.9940	26.89/0.8036	35.65/0.9417	47.84/0.9960	39.12/0.9338
	MSDTGP [19]	46.08/0.9939	26.75/0.8010	35.46/0.9409	47.39/0.9957	38.92/0.9329
	MANA [15]	46.02/0.9938	26.89/0.8040	35.51/0.9412	47.56/0.9957	39.01/0.9337
	BasicVSR [20]	46.13/0.9940	26.97/0.8059	35.54/0.9416	47.83/0.9959	39.12/0.9343
	TDMVSR (Ours)	46.20/0.9939	27.04/0.8084	35.54/0.9413	48.09/0.9960	39.22/0.9349

TABLE III. Quantitative comparisons on SkySat-1 and Zhuhai-1. The best and second performances are highlighted in red and blue, respectively.

Data Source	Scene	DUF-52L [18]	SOF-VSR [13]	RBPN [12]	MSDTGP [19]	EDVR-L [16]	MANA [15]	BasicVSR [20]	TDMVSR (Ours)
SkySat-1	Scene-14	33.77/0.9302	33.29/0.9255	33.79/0.9301	33.79/0.9317	33.98/0.9339	33.94/0.9331	34.00/0.9343	34.03/0.9360
	Scene-15	33.34/0.9136	32.92/0.9085	33.24/0.9123	33.23/0.9141	33.42/0.9157	33.27/0.9138	33.38/0.9144	33.66/0.9198
Zhuhai-1	Scene-16	32.85/0.9002	32.72/0.8976	32.71/0.8976	32.83/0.9004	32.85/0.9013	32.80/0.9003	32.80/0.9006	33.04/0.9048
	Average	33.32/0.9147	32.98/0.9105	33.25/0.9133	33.28/0.9154	33.42/0.9170	33.34/0.9157	33.39/0.9164	33.58/0.9202

this is because the recurrent propagation will inevitably accumulate the misalignment when the input frames increase and the scene variate. Thanks to the difference compensation unit, we can mitigate the misalignment by increasing the interaction between spatial-temporal information, thus maintaining spatial consistency and attaining the best performance in various scenes.

2) *Qualitative Results*: The visual comparison results are shown in Fig. 4, 5, and 6. In Fig. 4, TDMVSR can restore sharper and more reliable results. Specifically, in the scene2 of Jilin-1, UDF-52L, RBPN, and SOF-VSR produce blurred on the wing of the plane. It demonstrates neither 3D convolution nor optical flow is not enough to provide fine-grain temporal information. In scene-11 of Urthecast, DUF-52L and RBPN even predict the distortion lines. Here, EDVR-L, MSDTGP, and BasicVSR generate relatively correct lines. Nevertheless, their results are mixed and unclear enough compared with our

TDMVSR. In scene 8 of Carbonite-2, TDMVSR can preserve the reliable shape and edge of the elliptical marks on the building. As mentioned before, short-term temporal have high responses on the boundary of objects, and long-term difference maps focus on the edge and shape information. The visual comparison reveals that the proposed S-TDM and L-TDM could exploit this valuable high-frequency information and compensate them to the target frame.

In Fig. 5, TDMVSR can also restore the circular ground objects and line information for buildings. All the methods except BasicVSR and our TDMVSR recover the contorted results and severe artifacts. These results illustrate that TDMs can maintain the temporal consistency from the neighboring frames and avoid misalignment.

In Fig. 6, we zoomed and displayed the details on a scene of Zhuhai-1. TDMVSR obtained relatively realistic visual performance, while other approaches failed to recover the

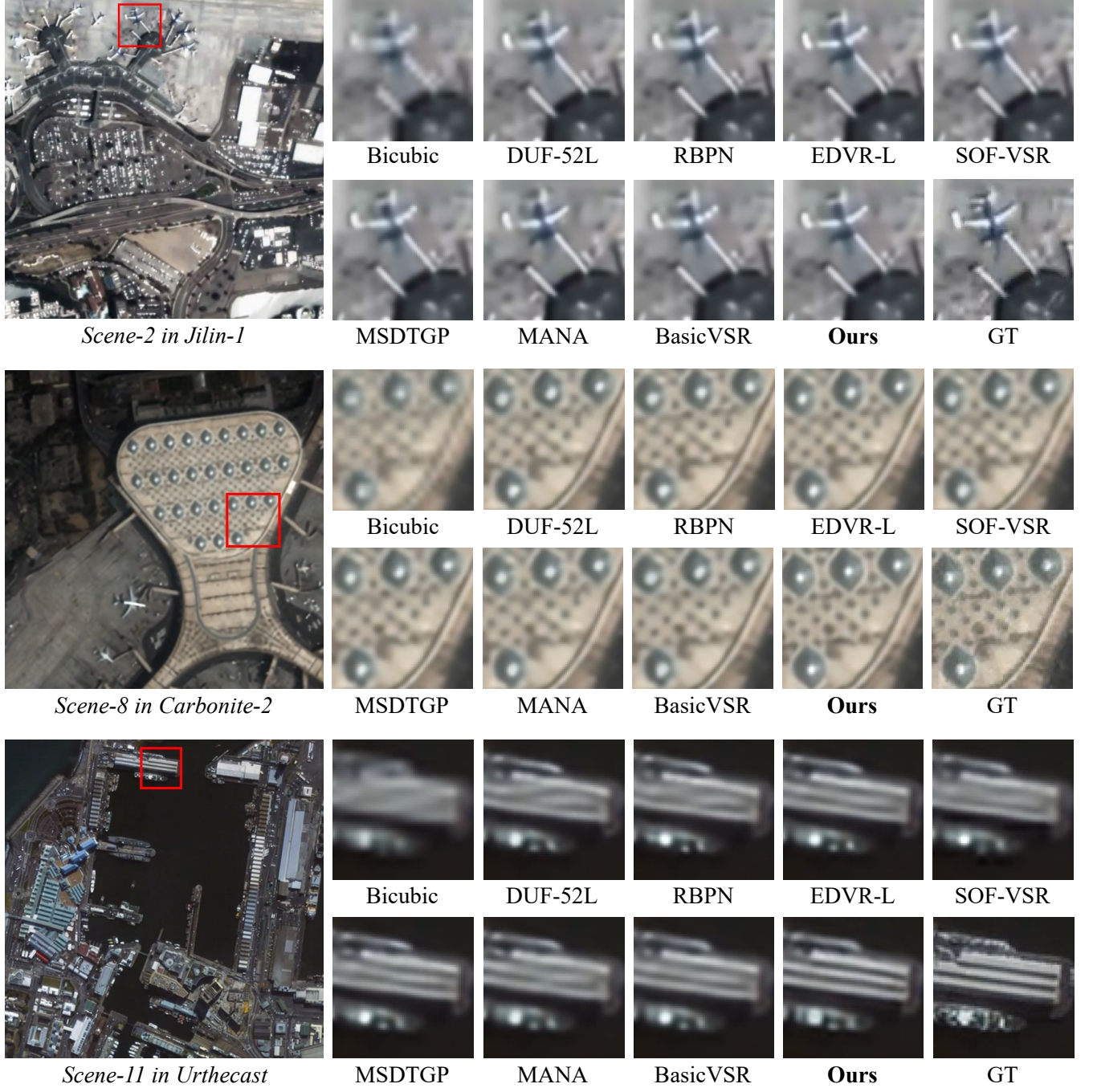


Fig. 4. Qualitative comparisons on scene-2 of Jilin-1, scene-8 of Carbonite-2, and scene-11 from Urthecast. Zoom in for better visualization.

high-frequency information. To better evaluate the temporal profile of each method, we record a line of pixels and stack them on the timeline. The temporal profile is shown in Fig. 7. More temporal details can be seen in our TDMVSR, which verifies that S-TDM and L-TDM can explore enriched information through temporal difference learning and recover a consistent profile with the ground truth.

D. Ablation Studies

In this section, we conducted several experiments to demonstrate the effectiveness of temporal difference learning. Note that the PSNR is calculated in scene-2 of Jinlin-T.

1) *The Number of Input Frames*: We investigate the input number of each model in Fig. 9. The PSNR is the average result of 16 scenes in five satellite videos. Besides, we change the frame length of our approach. TDMVSR- n means we adopt n consecutive frames as input. The results indicate that our TDMVSR can achieve the best performance in each condition. Therefore, we take five frames as input in the following experiments since TDMVSR-5 is the best.

2) *Effectiveness of S-TDM and L-TDM*: Firstly, we remove the L-TDM (Model-1) and S-TDM (Model-2) to investigate their contribution. The PSNR will decrease by 0.1dB if we do not conduct long-term temporal difference modeling. This

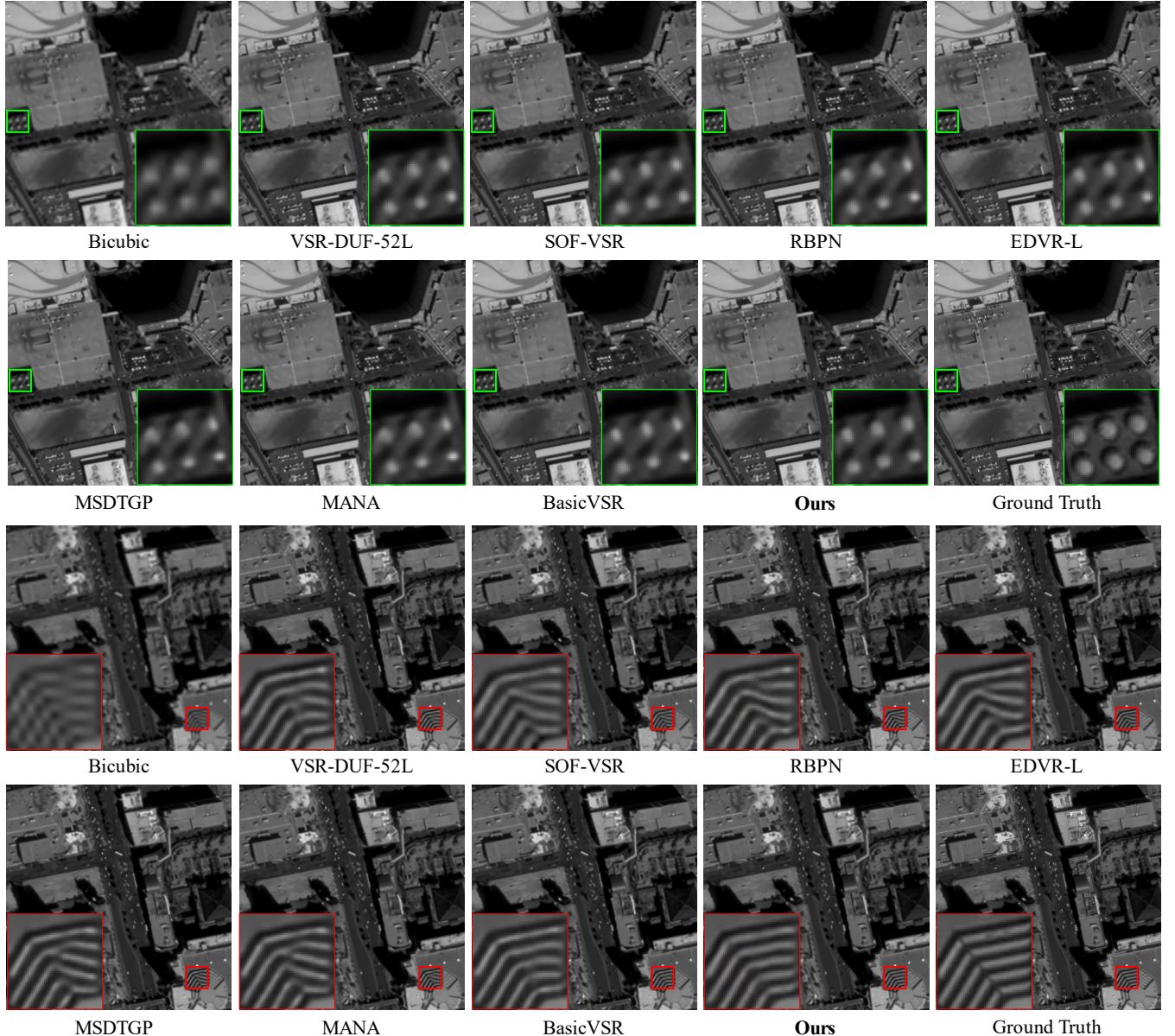


Fig. 5. Qualitative comparisons on scene-14 and scene-15 of SkySat-1. Zoom in for better visualization.

demonstrates L-TDM can provide valuable long-range dependency for temporal compensation.

3) *Effectiveness of Difference Operation*: To explore the effectiveness and efficiency of difference calculations on TDMs, we substitute the difference operation with naive concatenation. In particular, Model-3 directly concatenates the adjacent frames in S-TDM to extract the local temporal information. Model-4 stacks the forward and backward features in the channel dimension, then fuse them with a 3×3 convolution layer to extract the long-range dependency. Model-5 chooses to adopt concatenation in S-TDM and L-TDM simultaneously. The training process is shown in Fig. 8, and the PSNR performance of each is summarized in Table. V. It can be seen that simple concatenation will decrease the PSNR by 0.1dB while increasing the FLOPs (3.95G) and parameters (0.07M). Our TDMVSR can boost the efficiency and PSNR by conducting temporal difference in TDMs, which demon-

strates difference operation can reduce the high redundancy within satellite video and give an informative representation of motion information.

4) *Effectiveness of Bidirectional Difference*: We argue that our L-TDM can leverage the long-range temporal from forward and backward segments. Thus we set two models for comparisons: (1) Model-6 with only forward propagation; (2) Model-7 with only backward propagation. The PNSR results are in Table. VI. Compared with single forward architecture, bidirectional design help to improve 0.23dB with only a few FLOPs increase. On the one hand, it demonstrates that forward and backward features can provide complementary information. On the other hand, we can grasp cross-segment information with our bi-directional difference operation.

5) *Effectiveness of Difference Compensation Unit*: The restored HR target frame is required to maintain the spatial consistency of the LR target frame. Although S-TDM and

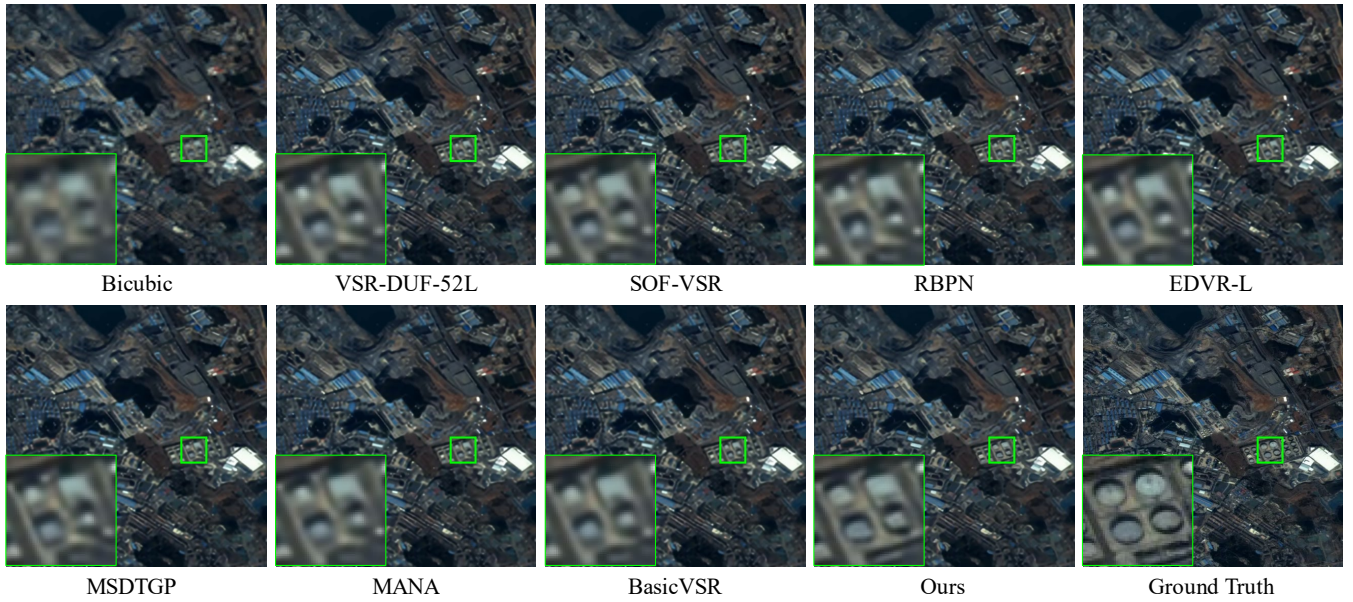


Fig. 6. Qualitative comparisons on scene-16 of Zhuhai-1. Zoom in for better visualization.

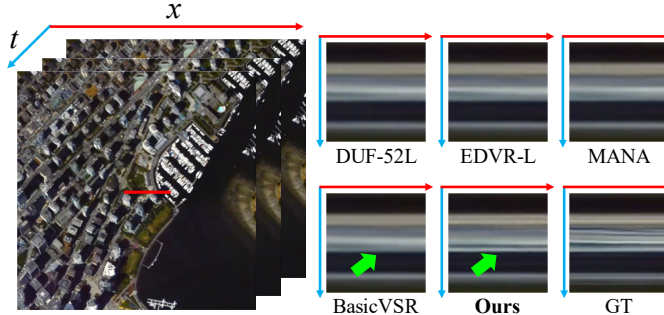


Fig. 7. Qualitative comparisons of temporal profile. Temporal profile is generated by recording a pixel line (red light) with stacking among frames.

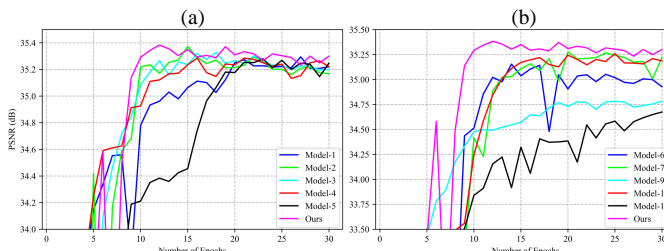


Fig. 8. The training process of different models. Model-1 and Model-2 are used for valid the effectiveness of S-TDM and L-TDM. Model-3 to Model-5 are designed to prove the effectiveness of difference operation. Model-6 and Model-7 are used to demonstrate the effectiveness of bidirectional propagation in L-TDM. Finally, Model-9 to Model-11 are established to indicate the effectiveness of hybrid attention.

L-TDM are capable of modeling temporal information for compensation, we still need to guide them to focus on the valuable compensation for the spatial feature and reduce the interference of misalignment. Therefore, we set Model-8 to remove the DCU and concatenate the temporal compensated feature with the spatial feature for spatial-temporal fusion. The results in Table. VII indicate that DCU can learn more useful temporal information to improve performance.

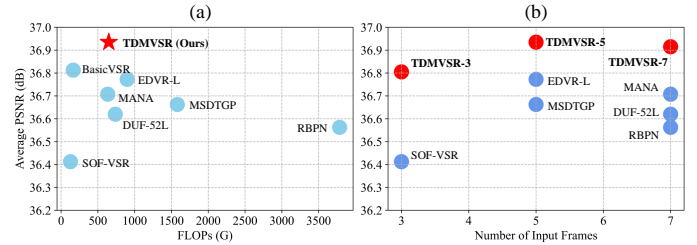


Fig. 9. (a) displays the relationship between FLOPs and PSNR of each model. (b) shows the relationship between input frame numbers and PSNR. Our TDMVSR achieves the best performance with acceptable FLOPs.

TABLE IV. Ablation experiment on the effectiveness of S-TDM and L-TDM. Results are calculated on scene 2 of Jilin-T in the Y channel.

Models	S-TMD	L-TMD	FLOPs	#Param.	PSNR (dB)
Model-1	✓		481.02	18.72	35.28
Model-2		✓	633.83	19.69	35.34
Ours	✓	✓	647.80	20.73	35.38

6) *Effectiveness of Hybrid Attention Reconstruction:* In our paper, two powerful attention mechanisms are adopted for the final reconstruction. We set a baseline model which uses the same number of residual blocks for reconstruction. Since the compensated feature is entangled with short-term and long-term temporal information, the residual block is struggled to reconstruct this complicated distribution. Although model-10 only adopts long-term attention and Model-11 considers short-term information, we can find that both Model-10 and Model-11 can bottleneck with partial consideration of long-short-term information. In summary, our hybrid attention design could comprehensively preserve long-short-term temporal information.

V. CONCLUSION

In this paper, we proposed a global-local temporal difference learning network to realize the short-term and long-term temporal compensation for satellite VSR. To explore

TABLE V. Ablation experiment on the effectiveness of difference operation. Results are calculated on scene 2 of Jilin-T in the Y channel.

Models	S-TDM	L-TDM	FLOPs	#Param.	PSNR (dB)
Model-3	Concat	Diff	647.98	20.73	35.33
Model-4	Diff	Concat	651.58	20.79	35.29
Model-5	Concat	concat	651.75	20.8	35.28
Ours	Diff	Diff	647.80	20.73	35.38

TABLE VI. Ablation experiment on the effectiveness of bidirectional difference. Results are calculated on scene 2 of Jilin-T in the Y channel.

Models	Forward	Backward	FLOPs	#Param.	PSNR (dB)
Model-6	✓		636.23	20.73	35.15
Model-7		✓	636.23	20.73	35.28
Ours	✓	✓	647.80	20.73	35.38

TABLE VII. Ablation experiment on the effectiveness of difference compensation unit. Results are calculated on scene 2 of Jilin-T in the Y channel.

Models	DF	DCU	FLOPs	#Param.	PSNR (dB)
Model-8	✓		641.18	20.47	35.31
Ours		✓	647.80	20.73	35.38

TABLE VIII. Ablation experiment on the effectiveness of hybrid attention reconstruction. Results are calculated on scene 2 of Jilin-T in the Y channel.

Models	Res-block	LA	SA	#Param.	PSNR (dB)
Model-9	✓			6.88	34.83
Model-10		✓		15.15	35.26
Model-11			✓	13.06	34.72
Ours		✓	✓	20.73	35.38

the local temporal information, we proposed to compute the frame-wise RGB difference between adjacent frames and supplied short-term temporal representation to target feature in a two-stage manner. To leverage the long-range dependency containing in the entire frames sequence, we design a bidirectional long-term temporal difference module. The holistic temporal difference is conducted on the smoothed forward and backward features to reduce the high redundancy. Then, the activated long-term attention is used to modulated the smoothed feature for compensation. Besides, we design a compensation unit to iterate the spatial-temporal for refinement. Extensive experiment on five mainstream satellite video demonstrate our TDMVSR can recover high fieldability compared with state-of-the-art methods.

In the future, we plan to design a lightweight attention mechanism to reconstruct spatio-temporal information. Since the introduction of hybrid attention significantly increases the number of parameters of our model.

REFERENCES

- [1] Y. Zhou, F. Wang, J. Zhao, R. Yao, S. Chen, and H. Ma, “Spatial-temporal based multihead self-attention for remote sensing image change detection,” *IEEE Transactions on Circuits and Systems for Video Technology*, vol. 32, no. 10, pp. 6615–6626, 2022.
- [2] M. Zhao, S. Li, S. Xuan, L. Kou, S. Gong, and Z. Zhou, “Satsot: A benchmark dataset for satellite video single object tracking,” *IEEE Transactions on Geoscience and Remote Sensing*, vol. 60, pp. 1–11, 2022.
- [3] S. He, M. A. Sadeghi, S. Chawla, M. Alizadeh, H. Balakrishnan, and S. Madden, “Inferring high-resolution traffic accident risk maps based on satellite imagery and gps trajectories,” in *Proceedings of the IEEE/CVF International Conference on Computer Vision*, 2021, pp. 11977–11985.
- [4] A. Niu, Y. Zhu, C. Zhang, J. Sun, P. Wang, I. S. Kweon, and Y. Zhang, “Ms2net: Multi-scale and multi-stage feature fusion for blurred image super-resolution,” *IEEE Transactions on Circuits and Systems for Video Technology*, vol. 32, no. 8, pp. 5137–5150, 2022.
- [5] C. Wang, J. Jiang, Z. Zhong, and X. Liu, “Propagating facial prior knowledge for multitask learning in face super-resolution,” *IEEE Transactions on Circuits and Systems for Video Technology*, vol. 32, no. 11, pp. 7317–7331, 2022.
- [6] M. Liu, S. Jin, C. Yao, C. Lin, and Y. Zhao, “Temporal consistency learning of inter-frames for video super-resolution,” *IEEE Transactions on Circuits and Systems for Video Technology*, pp. 1–13, 2022.
- [7] K. Sun, M. Koch, Z. Wang, S. Jovanovic, H. Rabah, and S. Simon, “An fpga-based residual recurrent neural network for real-time video super-resolution,” *IEEE Transactions on Circuits and Systems for Video Technology*, vol. 32, no. 4, pp. 1739–1750, 2021.
- [8] W. Wen, W. Ren, Y. Shi, Y. Nie, J. Zhang, and X. Cao, “Video super-resolution via a spatio-temporal alignment network,” *IEEE Transactions on Image Processing*, vol. 31, pp. 1761–1773, 2022.
- [9] D. Zhang, J. Shao, Z. Liang, X. Liu, and H. T. Shen, “Multi-branch networks for video super-resolution with dynamic reconstruction strategy,” *IEEE Transactions on Circuits and Systems for Video Technology*, vol. 31, no. 10, pp. 3954–3966, 2020.
- [10] Y. Zhang, H. Wang, H. Zhu, and Z. Chen, “Optical flow reusing for high-efficiency space-time video super resolution,” *IEEE Transactions on Circuits and Systems for Video Technology*, 2022.
- [11] P. Yi, Z. Wang, K. Jiang, Z. Shao, and J. Ma, “Multi-temporal ultra dense memory network for video super-resolution,” *IEEE Transactions on Circuits and Systems for Video Technology*, vol. 30, no. 8, pp. 2503–2516, 2019.
- [12] M. Haris, G. Shakhnarovich, and N. Ukita, “Recurrent back-projection network for video super-resolution,” in *Proceedings of the IEEE/CVF Conference on Computer Vision and Pattern Recognition*, 2019, pp. 3897–3906.
- [13] L. Wang, Y. Guo, L. Liu, Z. Lin, X. Deng, and W. An, “Deep video super-resolution using hr optical flow estimation,” *IEEE Transactions on Image Processing*, vol. 29, pp. 4323–4336, 2020.
- [14] Y. Xiao, Q. Yuan, J. He, Q. Zhang, J. Sun, X. Su, J. Wu, and L. Zhang, “Space-time super-resolution for satellite video: A joint framework based on multi-scale spatial-temporal transformer,” *International Journal of Applied Earth Observation and Geoinformation*, vol. 108, p. 102731, 2022.
- [15] J. Yu, J. Liu, L. Bo, and T. Mei, “Memory-augmented non-local attention for video super-resolution,” in *Proceedings of the IEEE/CVF Conference on Computer Vision and Pattern Recognition*, 2022, pp. 17834–17843.
- [16] X. Wang, K. C. Chan, K. Yu, C. Dong, and C. Change Loy, “Edvr: Video restoration with enhanced deformable convolutional networks,” in *Proceedings of the IEEE/CVF Conference on Computer Vision and Pattern Recognition Workshops*, 2019, pp. 0–0.
- [17] T. Isobe, S. Li, X. Jia, S. Yuan, G. Slabaugh, C. Xu, Y.-L. Li, S. Wang, and Q. Tian, “Video super-resolution with temporal group attention,” in *Proceedings of the IEEE/CVF conference on computer vision and pattern recognition*, 2020, pp. 8008–8017.
- [18] Y. Jo, S. W. Oh, J. Kang, and S. J. Kim, “Deep video super-resolution network using dynamic upsampling filters without explicit motion compensation,” in *Proceedings of the IEEE conference on computer vision and pattern recognition*, 2018, pp. 3224–3232.
- [19] Y. Xiao, X. Su, Q. Yuan, D. Liu, H. Shen, and L. Zhang, “Satellite video super-resolution via multiscale deformable convolution alignment and temporal grouping projection,” *IEEE Transactions on Geoscience and Remote Sensing*, vol. 60, pp. 1–19, 2022.
- [20] K. C. Chan, X. Wang, K. Yu, C. Dong, and C. C. Loy, “Basicvsr: The search for essential components in video super-resolution and beyond,” in *Proceedings of the IEEE/CVF Conference on Computer Vision and Pattern Recognition*, 2021, pp. 4947–4956.
- [21] P. Yi, Z. Wang, K. Jiang, J. Jiang, T. Lu, X. Tian, and J. Ma, “Omniscient video super-resolution,” in *Proceedings of the IEEE/CVF International Conference on Computer Vision*, 2021, pp. 4429–4438.
- [22] J. Zhu, Q. Zhang, L. Fei, R. Cai, Y. Xie, B. Sheng, and X. Yang, “Fffn: Frame-by-frame feedback fusion network for video super-resolution,” *IEEE Transactions on Multimedia*, 2022.
- [23] Y. Zhao, Y. Xiong, and D. Lin, “Recognize actions by disentangling components of dynamics,” in *Proceedings of the IEEE Conference on Computer Vision and Pattern Recognition*, 2018, pp. 6566–6575.
- [24] L. Wang, Y. Xiong, Z. Wang, Y. Qiao, D. Lin, X. Tang, and L. Van Gool, “Temporal segment networks: Towards good practices for deep action recognition,” in *European conference on computer vision*. Springer, 2016, pp. 20–36.

[25] R. Liao, X. Tao, R. Li, Z. Ma, and J. Jia, "Video super-resolution via deep draft-ensemble learning," in *Proceedings of the IEEE international conference on computer vision*, 2015, pp. 531–539.

[26] T. Brox, A. Bruhn, N. Papenberg, and J. Weickert, "High accuracy optical flow estimation based on a theory for warping," in *European conference on computer vision*. Springer, 2004, pp. 25–36.

[27] A. Kappeler, S. Yoo, Q. Dai, and A. K. Katsaggelos, "Video super-resolution with convolutional neural networks," *IEEE transactions on computational imaging*, vol. 2, no. 2, pp. 109–122, 2016.

[28] M. Drulea and S. Nedevschi, "Total variation regularization of local-global optical flow," in *2011 14th International IEEE Conference on Intelligent Transportation Systems (ITSC)*. IEEE, 2011, pp. 318–323.

[29] C. Liu *et al.*, "Beyond pixels: exploring new representations and applications for motion analysis," Ph.D. dissertation, Massachusetts Institute of Technology, 2009.

[30] J. Caballero, C. Ledig, A. Aitken, A. Acosta, J. Totz, Z. Wang, and W. Shi, "Real-time video super-resolution with spatio-temporal networks and motion compensation," in *Proceedings of the IEEE conference on computer vision and pattern recognition*, 2017, pp. 4778–4787.

[31] E. Ilg, N. Mayer, T. Saikia, M. Keuper, A. Dosovitskiy, and T. Brox, "FlowNet 2.0: Evolution of optical flow estimation with deep networks," in *Proceedings of the IEEE conference on computer vision and pattern recognition*, 2017, pp. 2462–2470.

[32] A. Ranjan and M. J. Black, "Optical flow estimation using a spatial pyramid network," in *Proceedings of the IEEE conference on computer vision and pattern recognition*, 2017, pp. 4161–4170.

[33] S. Y. Kim, J. Lim, T. Na, and M. Kim, "Video super-resolution based on 3d-cnns with consideration of scene change," in *2019 IEEE International Conference on Image Processing (ICIP)*. IEEE, 2019, pp. 2831–2835.

[34] P. Yi, Z. Wang, K. Jiang, J. Jiang, T. Lu, and J. Ma, "A progressive fusion generative adversarial network for realistic and consistent video super-resolution," *IEEE Transactions on Pattern Analysis and Machine Intelligence*, 2020.

[35] J. Dai, H. Qi, Y. Xiong, Y. Li, G. Zhang, H. Hu, and Y. Wei, "Deformable convolutional networks," in *Proceedings of the IEEE international conference on computer vision*, 2017, pp. 764–773.

[36] Y. Tian, Y. Zhang, Y. Fu, and C. Xu, "Tdan: Temporally-deformable alignment network for video super-resolution," in *Proceedings of the IEEE/CVF Conference on Computer Vision and Pattern Recognition*, 2020, pp. 3360–3369.

[37] X. Ying, L. Wang, Y. Wang, W. Sheng, W. An, and Y. Guo, "Deformable 3d convolution for video super-resolution," *IEEE Signal Processing Letters*, vol. 27, pp. 1500–1504, 2020.

[38] Y. Huang, W. Wang, and L. Wang, "Video super-resolution via bidirectional recurrent convolutional networks," *IEEE transactions on pattern analysis and machine intelligence*, vol. 40, no. 4, pp. 1015–1028, 2017.

[39] X. Tao, H. Gao, R. Liao, J. Wang, and J. Jia, "Detail-revealing deep video super-resolution," in *Proceedings of the IEEE International Conference on Computer Vision*, 2017, pp. 4472–4480.

[40] J. Guo and H. Chao, "Building an end-to-end spatial-temporal convolutional network for video super-resolution," in *Thirty-First AAAI Conference on Artificial Intelligence*, 2017.

[41] X. Zhu, Z. Li, X.-Y. Zhang, C. Li, Y. Liu, and Z. Xue, "Residual invertible spatio-temporal network for video super-resolution," in *Proceedings of the AAAI conference on artificial intelligence*, vol. 33, no. 01, 2019, pp. 5981–5988.

[42] K. C. Chan, S. Zhou, X. Xu, and C. C. Loy, "Basicvsr++: Improving video super-resolution with enhanced propagation and alignment," in *Proceedings of the IEEE/CVF Conference on Computer Vision and Pattern Recognition*, 2022, pp. 5972–5981.

[43] Y. Luo, L. Zhou, S. Wang, and Z. Wang, "Video satellite imagery super resolution via convolutional neural networks," *IEEE Geoscience and Remote Sensing Letters*, vol. 14, no. 12, pp. 2398–2402, 2017.

[44] K. Jiang, Z. Wang, P. Yi, G. Wang, T. Lu, and J. Jiang, "Edge-enhanced gan for remote sensing image superresolution," *IEEE Transactions on Geoscience and Remote Sensing*, vol. 57, no. 8, pp. 5799–5812, 2019.

[45] S. Zhang, Q. Yuan, J. Li, J. Sun, and X. Zhang, "Scene-adaptive remote sensing image super-resolution using a multiscale attention network," *IEEE Transactions on Geoscience and Remote Sensing*, vol. 58, no. 7, pp. 4764–4779, 2020.

[46] Z. He and D. He, "A unified network for arbitrary scale super-resolution of video satellite images," *IEEE Transactions on Geoscience and Remote Sensing*, vol. 59, no. 10, pp. 8812–8825, 2020.

[47] H. Liu, Y. Gu, T. Wang, and S. Li, "Satellite video super-resolution based on adaptively spatiotemporal neighbors and nonlocal similarity regularization," *IEEE Transactions on Geoscience and Remote Sensing*, vol. 58, no. 12, pp. 8372–8383, 2020.

[48] Z. He, J. Li, L. Liu, D. He, and M. Xiao, "Multiframe video satellite image super-resolution via attention-based residual learning," *IEEE Transactions on Geoscience and Remote Sensing*, vol. 60, pp. 1–15, 2021.

[49] Y. Zhang, K. Li, K. Li, L. Wang, B. Zhong, and Y. Fu, "Image super-resolution using very deep residual channel attention networks," in *Proceedings of the European conference on computer vision (ECCV)*, 2018, pp. 286–301.

[50] J. Liang, J. Cao, G. Sun, K. Zhang, L. Van Gool, and R. Timofte, "Swinir: Image restoration using swin transformer," in *Proceedings of the IEEE/CVF International Conference on Computer Vision*, 2021, pp. 1833–1844.

[51] X. Chen, X. Wang, J. Zhou, and C. Dong, "Activating more pixels in image super-resolution transformer," *arXiv preprint arXiv:2205.04437*, 2022.

Yi Xiao received the B.S. degree from the School of Mathematics and Physics, China University of Geosciences, Wuhan, China, in 2020. He is pursuing the Ph.D. degree with the School of Geodesy and Geomatics, Wuhan University, Wuhan.

His major research interests are remote sensing image super-resolution and computer vision. More details can be found at <https://xy-boy.github.io/>



Qiangqiang Yuan (Member, IEEE) received the B.S. degree in surveying and mapping engineering and the Ph.D. degree in photogrammetry and remote sensing from Wuhan University, Wuhan, China, in 2006 and 2012, respectively.

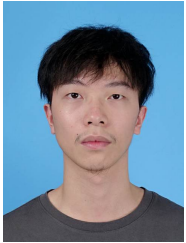
In 2012, he joined the School of Geodesy and Geomatics, Wuhan University, where he is a Professor. He has published more than 90 research papers, including more than 70 peer-reviewed articles in international journals, such as *Remote Sensing of Environment*, *ISPRS Journal of Photogrammetry and Remote Sensing*, *IEEE TRANSACTION ON IMAGE PROCESSING*, and *IEEE TRANSACTIONS ON GEOSCIENCE AND REMOTE SENSING*. His research interests include image reconstruction, remote sensing image processing and application, and data fusion.

Dr. Yuan was a recipient of the Youth Talent Support Program of China in 2019, the Top-Ten Academic Star of Wuhan University in 2011, and the recognition of Best Reviewers of the IEEE GRSL in 2019. In 2014, he received the Hong Kong Scholar Award from the Society of Hong Kong Scholars and the China National Postdoctoral Council. He is an associate editor of 5 international journals and has frequently served as a referee for more than 40 international journals for remote sensing and image processing.



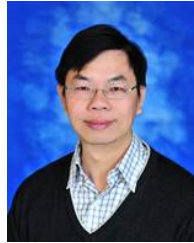
Kui Jiang (Member, IEEE) received the Ph.D. degree in the School of Computer Science, Wuhan University, Wuhan, China, in 2022. Dr. Jiang is now a Chief Engineer with Huawei Technologies, Cloud BU, Hangzhou, China. He received the 2022 ACM Wuhan Doctoral Dissertation Award.

His research interests include image/video processing and computer vision.



Xianyu Jin received the B.S. degree in geodesy and geomatics engineering from Wuhan University, Wuhan, China, in 2019, where he is pursuing the M.S. degree with the School of Geodesy and Geomatics.

His research interests include video super-resolution, deep learning, and computer vision.



Chia-Wen Lin (Fellow, IEEE) received the Ph.D degree in electrical engineering from National Tsing Hua University (NTHU), Hsinchu, Taiwan, in 2000. He is currently Professor with the Department of Electrical Engineering and the Institute of Communications Engineering, NTHU. He is also Deputy Director of the AI Research Center of NTHU. He was with the Department of Computer Science and Information Engineering, National Chung Cheng University, Taiwan, during 2000–2007. Prior to joining academia, he worked for the Information and Communications Research Laboratories, Industrial Technology Research Institute, Hsinchu, Taiwan, during 1992–2000. His research interests include image and video processing, computer vision, and video networking.

Dr. Lin served as Distinguished Lecturer of IEEE Circuits and Systems Society from 2018 to 2019, a Steering Committee member of IEEE TRANSACTIONS ON MULTIMEDIA from 2014 to 2015, and the Chair of the Multimedia Systems and Applications Technical Committee of the IEEE Circuits and Systems Society from 2013 to 2015. His articles received the Best Paper Award of IEEE VCIP 2015 and the Young Investigator Award of VCIP 2005. He received Outstanding Electrical Professor Award presented by Chinese Institute of Electrical Engineering in 2019, and Young Investigator Award presented by Ministry of Science and Technology, Taiwan, in 2006. He is also the Chair of the Steering Committee of IEEE ICME. He has served as a Technical Program Co-Chair for IEEE ICME 2010, and a General Co-Chair for IEEE VCIP 2018, and a Technical Program Co-Chair for IEEE ICIP 2019. He has served as an Associate Editor of IEEE TRANSACTIONS ON IMAGE PROCESSING, IEEE TRANSACTIONS ON CIRCUITS AND SYSTEMS FOR VIDEO TECHNOLOGY, IEEE TRANSACTIONS ON MULTIMEDIA, IEEE MULTIMEDIA, and Journal of Visual Communication and Image Representation.



Jiang He received the B.S. degree in remote sensing science and technology from faculty of geosciences and environmental engineering in Southwest Jiaotong University, Chengdu, China, in 2018. He is currently pursuing the Ph.D. degree in School of Geodesy and Geomatics, Wuhan University, Wuhan, China.

His research interests include hyperspectral super-resolution, image fusion, quality improvement, remote sensing image processing and deep learning.



Liangpei Zhang (Fellow, IEEE) received the B.S. degree in physics from Hunan Normal University, Changsha, China, in 1982, the M.S. degree in optics from the Xi'an Institute of Optics and Precision Mechanics, Chinese Academy of Sciences, Xi'an, China, in 1988, and the Ph.D. degree in photogrammetry and remote sensing from Wuhan University, Wuhan, China, in 1998.

He is currently a “Chang-Jiang Scholar” Chair Professor appointed by the Ministry of Education of China at the State Key Laboratory of Information Engineering in Surveying, Mapping, and Remote Sensing (LIESMARS), Wuhan University. He was a Principal Scientist for the China State Key Basic Research Project from 2011 to 2016 appointed by the Ministry of National Science and Technology of China to lead the Remote Sensing Program in China. He has published more than 700 research articles and five books. He is the Institute for Scientific Information (ISI) Highly Cited Author. He holds 30 patents. His research interests include hyperspectral remote sensing, highresolution remote sensing, image processing, and artificial intelligence.

Dr. Zhang is a fellow of the Institution of Engineering and Technology (IET). He was a recipient of the 2010 Best Paper Boeing Award, the 2013 Best Paper ERDAS Award from the American Society of Photogrammetry and Remote Sensing (ASPRS), and the 2016 Best Paper Theoretical Innovation Award from the International Society for Optics and Photonics (SPIE). His research teams won the top three prizes of the IEEE GRSS 2014 Data Fusion Contest. His students have been selected as the winners or finalists of the IEEE International Geoscience and Remote Sensing Symposium (IGARSS) Student Paper Contest in recent years. He is also the Founding Chair of the IEEE Geoscience and Remote Sensing Society (GRSS) Wuhan Chapter. He also serves as an associate editor or an editor for more than ten international journals. He is also serving as an Associate Editor for the IEEE TRANSACTIONS ON GEOSCIENCE AND REMOTE SENSING.